ADVANCED OPTICAL MATERIALS
www.advopticalmat.de

Site-Engineering for Controlling Multiple-Excitation and Emission in Eu^{2+}-Activated $CaSrSiO_4$ Phosphors in Marine Fisheries

Shuifu Liu, Dawei Wen, Rongkai Du, Chunyan Jiang, Jun Chen, Junhao Li, Lei Zhou, Maxim S. Molokeev, and Mingmei Wu**

Artificial light fishing technology has been used in marine fisheries for thousands of years. The light source with multi-color adjustable output is expected to become a new generation of fish-attracting lamps. Herein, a new method of crystal-site engineering through reducing atmospheres is proposed for the development of Eu^{2+} doped single-phase phosphor with multi-excitation and multi-emission properties. Following this approach, the distribution ratio of Eu^{2+} at Ca^{2+} and Sr^{2+} sites in $CaSrSiO_4$ (CSO) can be modulated. Importantly, Eu^{2+} at both lattice sites exhibit non-interfering optical properties, CSO:Eu^{2+} phosphor realizes multi-color output from green to yellow and then to red when Eu^{2+} occupies the Sr^{2+} and Ca^{2+} sites in a relatively balanced ratio. Benefitting from the tunable color range covering the spectral sensitivity regions of most marine fishes, this phosphor may eventually be applied in futuristic innovative fish-attracting lamps.

1. Introduction

The trapping of fish at night with artificial light according to the phototropism of fish is an important technique in marine fishing, which has been employed for thousands of years.[1] Initially, humans discovered that torches could be used to illuminate fishing work at night while simultaneously attracting fish. Subsequently, fishing with light has emerged as an advanced and efficient industrial approach to catching commercially important fish species. With the development of society and technology, fish-attracting lamps have undergone a process of renewal from paraffin lamps, tungsten strip lamps, metal halide lamps, and incandescent lamps to light-emitting diode (LED) lamps.[2] At present, white LEDs have become the mainstream fish-attracting lamp light source owing to their low energy consumption, long operating lifetime and environmental friendliness, etc.[3] However, there are differences in the phototropism of the various species of fish to light. For example, squid, pointhead flounder, and masked greenling are sensitive to green, yellow, and red light, respectively.[4] Therefore, traditional white light sources are not the best option for fish-attracting lamps, as the redundant spectral components of white light sources will result in energy loss and may scare fish. Alternatively, fish-attracting lamps with color-adjustable output depending on the target fish species have the advantage of being more targeted and more energy-saving.[5] Unfortunately, the development of such fish-attracting lamps is still a challenge.

It is well known that the phosphor, as an important component part of the LED device, determines the light color output of the LED device. Single-phase phosphors with multi-excitation and emission properties are ideal candidates for the construction of futuristic innovative fish-attracting lamps with tunable light color output. At present, the development of single-phase phosphors with multi-excitation and emission properties is generally based on a combination of multiple dopants.[6] Although this method is simple and effective, single-phase phosphors doped with multiple dopants are often accompanied by low efficiency and poor color stability.[7] In contrast, a single-phase phosphor with a single activator that can be multi-color tunable output is a more ideal option due to its more prominent color stability as well as higher efficiency.

S. Liu, R. Du, C. Jiang, J. Chen, L. Zhou, M. Wu
School of Marine Sciences/School of Chemical Engineering and Technology/School of Chemistry
Sun Yat-sen University
519082/Guangzhou, Zhuhai 510006, P. R. China
E-mail: zhoul8@mail.sysu.edu.cn; ceswmm@mail.sysu.edu.cn

D. Wen
School of Applied Physics and Materials
WuYi University
Jiangmen 529020, P. R. China

J. Li
Guangdong Province Key Laboratory of Rare Earth Development and Application, Institute of Rare Metals
Guangdong Academy of Sciences
Guangzhou 510651, P. R. China

M. S. Molokeev
Laboratory of Crystal Physics
Kirensky Institute of Physics Federal Research Center KSC SB RAS
660036 Krasnoyarsk, Russia

M. S. Molokeev
Department of Engineering Physics and Radioelectronics
Siberian Federal University
660041 Krasnoyarsk, Russia

M. S. Molokeev
Department of Physics
Far Eastern State Transport University
680021 Khabarovsk, Russia

The ORCID identification number(s) for the author(s) of this article can be found under https://doi.org/10.1002/adom.202203151.

DOI: 10.1002/adom.202203151

Among the numerous activating ions, such as lanthanide ions and transition metal ions,[8] Eu^{2+} may be a more desirable activating ion for the development of single-phase phosphors with multi-excitation and emission properties. Eu^{2+} is typical of the 4f-5d transitions, which are characterized by high luminescence efficiency and sensitivity to the local structural environment.[9] The luminescence of Eu^{2+} covers the entire visible region and even extends to the NIR region.[10] Theoretically, Eu^{2+} occupying lattice sites in different coordination environments possess different excitation and emission characteristics, thus, have the potential to enable multi-excitation and emission of a single-phase phosphor. Nevertheless, owing to factors such as ionic radius, chemical valence, and polyhedral size, Eu^{2+} is usually preferentially occupied in a more suitable site, leading to phosphors exhibiting fixed-emitting color characteristics.[11] In recent years, it has been reported that some crystal-site engineering methods can well regulate the distribution of Eu^{2+} on multiple cationic sites in the matrix lattice.[12] However, even though Eu^{2+} is simultaneously distributed in more than one site with different local coordination environments, the similar coordination environment and the interactions between Eu^{2+} in these sites, such as energy transfer, will lead to a significant overlap of the excitation spectra, and limits the tunable range of light colors.[13] Therefore, the design of single-phase phosphors doped with a single activating ion with multi-excitation and multi-emission properties requires a rational regulation of the distribution of Eu^{2+} in different cationic sites. Simultaneously, the Eu^{2+} distributed on these sites should have optical properties that do not interfere with each other.

Herein, we present a crystal-site engineering method to develop Eu^{2+} activated single-phase phosphor with multi-excitation and emission characteristics. Our strategy breaks the tendency of Eu^{2+} to preferentially occupy suitable sites and induces Eu^{2+} into the disliked sites by simply reducing atmosphere modification. Eu^{2+} is designed with a suitable ratio to enter two sites with different coordination environments. Due to the non-interfering luminescent properties of Eu^{2+} at these sites, CSO:Eu^{2+} phosphors featuring a wide range of multicolor tunable output by manipulating the excitation wavelength are achieved. The tunable range of light colors covers the spectrally sensitive range of most marine economic fish, which means that CSO:Eu^{2+} phosphors prepared by this method have great potential for application in fish-attracting lamps. The mechanism behind reducing atmosphere-related luminescence tunability is revealed by experimental analysis and DFT calculation. The results suggest that Eu^{3+} plays an important role in the crystal site engineering of Eu^{2+} in CSO. This work not only proposes a peculiar site-selective modulation method that is valuable for phosphor design but also points to a new application direction for phosphors.

2. Results and Discussion

In this work, α'L-$CaSrSiO_4$ (α'L-CSO) is selected as the host material for the synthesis of Eu^{2+} doped phosphors. α'L-CSO belongs to the orthorhombic crystal structure with a space group of $Pna2_1$.[14] **Figure 1**a shows the crystal structure of α'L-CSO. There are three kinds of Sr (Sr1, Sr2, and Sr3) and Ca (Ca1, Ca2, and Ca3) sites in the α'L-CSO, respectively. All of the Sr is surrounded by ten O atoms to form SrO_{10} polyhedrons, and these polyhedrons are interconnected by vertex- and face-sharing with the SiO_4 tetrahedra (Figure S1, Supporting

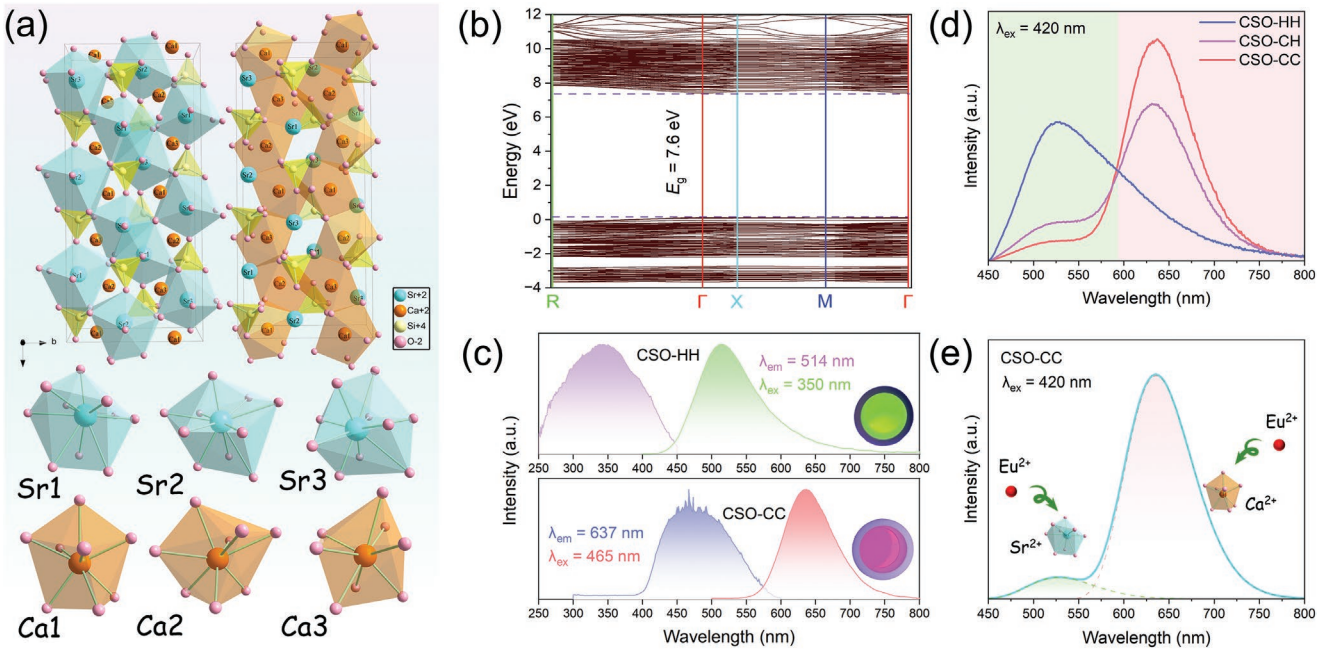

Figure 1. a) Crystal structure of CSO and the coordination polyhedrons of Sr and Ca. b) Calculated energy band structure of CSO. c) PLE and PL spectra of CSO-HH and CSO-CC. The insets show the digital photographs of CSO-HH and CSO-CC under UV and blue light excitation, respectively. d) PL spectra of CSO-HH, CSO-CH, and CSO-CC under 420 nm excitation. e) Gaussian fitting PL spectrum of CSO-CC.

Information). Three kinds of CaO_8 polyhedrons formed by linking with eight O atoms are connected to each other in the form of shared vertices and faces. SrO_{10} and CaO_8 polyhedrons are associated with each other by means of shared vertices or faces.

CSO:Eu^{2+} phosphors were prepared under three different reducing atmospheric conditions; the detailed experimental procedure is described in the section "Materials and Synthesis" in the Supporting Information and is graphically illustrated in Figure S2, Supporting Information. The sample prepared under hydrogen atmosphere and with subsequent re-sintering under hydrogen atmosphere is denoted as CSO-HH, while those prepared under thermal-carbon atmosphere and with subsequent re-sintering under hydrogen and thermal-carbon atmosphere respectively are denoted as CSO-CH and CSO-CC, respectively. To characterize the structure of the synthesized samples, α'L-CSO (ICDD #01-072-2260) was taken as the initial structure model for Rietveld refinement using TOPAS 4.2 (Figure S3, Supporting Information). The relevant Rietveld refinement data are listed in Table S1, Supporting Information. Refinements were stable and gave low *R*-factors, showing the credibility of the results. The microscopic morphology and elemental distribution of the synthesized samples were characterized by SEM and EDS (Figure S4a, Supporting Information). The sample powder exhibits a smooth surface and particle size of around 10 μm. In addition, EDS mapping images reveal a homogeneous distribution of elements in the samples. The fine structure and crystallinity properties of CSO:Eu^{2+} phosphors are further characterized via a high-resolution transmission electron microscopy (HRTEM) as shown in Figure S4b, Supporting Information. The HRTEM image shows clear and continuous lattice fringes with d-spacings of 0.2550 and 0.3222 nm, correlating well with the (331) and (321) lattice planes of α'L-CSO, respectively.

The band-gap structure of α'L-CSO has been calculated via the density functional theory (DFT) calculation (Figure 1b). The band gap value for α'L-CSO is calculated to be around 7.6 eV. The band structure and atomic orbital contributions in the valence and conduction bands are also revealed by the total and partial density of states (Figure S5, Supporting Information). Further, the host exciton absorption band of the α'L-CSO is detected by synchrotron vacuum ultraviolet-ultraviolet (VUV-UV) excitation spectrum, as displayed in Figure S6, Supporting Information. The asymmetric band with the maximum peak at around 170 nm (7.3 eV) originates from the host exciton absorption. Taking into account the electron-hole binding energy of the exciton, the band gap of α'L-CSO can be estimated as $1.08 \times 7.3 = 7.9$ eV.[15] The experimental band gap values are close to the theoretically calculated values (7.6 eV). This result implies that α'L-CSO is a suitable host material for phosphors to accommodate the ground and excited states of Eu^{2+} in its wide band gap.

Different luminescence in CSO:Eu^{2+} is found in the different reducing atmospheres. The insets of Figure 1c display that CSO-HH and CSO-CC phosphors present green and red colors under near-ultraviolet (about 365 nm) and blue (about 450 nm) light excitation, respectively. The normalized photoluminescence excitation (PLE) and photoluminescence emission (PL) spectra of CSO-HH and CSO-CC are presented in Figure 1c. CSO-HH shows green emission with the maximum emission peak at 514 nm under the excitation from 250 to 450 nm. Interestingly, CSO-CC mainly presents a red emission ranging from 550 to 800 nm with the strongest emission at around 637 nm under 465 nm excitation. In addition, CSO-HH can be detected with faint red emission under 465 nm excitation and CSO-CC exhibits weak green emission under 350 nm excitation (Figure S7, Supporting Information). Previously it was reported that CSO:Eu^{2+} was a typical yellow-green emitting phosphor,[16] while, herein, its red-emitting potential has been successfully activated (CSO-CC). This difference in luminescence characteristics indicates that Eu^{2+} is distributed to different cationic sites (either Sr^{2+} or Ca^{2+}), corresponding to two types of luminous centers. Figure 1d shows the emission spectra of CSO-HH, CSO-CH, and CSO-CC under 420 nm excitation. The emission spectra profiles of the CSO:Eu^{2+} synthesized under different reducing atmospheres show significant differences. The spectrum of CSO-HH covers mainly the green light region, while CSO-CH and CSO-CC are mainly concentrated in the red light region. The red emission intensity of CSO-CC is higher than that of CSO-CH, and the green emission intensity is weaker than that of CSO-CH. Similar phenomena can be observed in the emission spectra at other excitation wavelengths (Figure S8, Supporting Information). Under 350 nm excitation, the intensity of green emission varies as follows: CSO-HH > CSO-CH > CSO-CC, while under 465 nm excitation, the intensity of red emission shows the opposite trend. These spectral variations indicate that the distribution of Eu^{2+} at lattice sites can be modified by the reducing atmosphere. For α'L-CSO, the three types of Sr^{2+} sites have similar local coordination environments due to the same coordination number (CN = 10) and similar Sr-O bond lengths (Table S2, Supporting Information). Analogously, the sites of the three types of Ca^{2+} are roughly identical. The average bond length of Ca-O is shorter than that of Sr-O (Table S2, Supporting Information), meanwhile, the Ca^{2+} (CN = 8) has a lower coordination number than Sr^{2+} (CN = 10), suggesting a stronger crystal field strength.[17] The Eu^{2+} occupying the Ca^{2+} site suffers from a stronger crystal field splitting effect, resulting in longer wavelength emission. Therefore, it is concluded that the green emission originates from Eu^{2+} occupying the Sr^{2+} site whereas the red emission from Eu^{2+} at the Ca^{2+} site (Figure 1e).

To elucidate the origin of the different luminescence characteristics of CSO:Eu^{2+} phosphors, the distribution of Eu^{2+} on the cationic sites was investigated. The XRD patterns of the CSO:Eu^{2+} phosphors synthesized under different reducing atmospheres are displayed in **Figure 2**a, all of them can be indexed with the α'L-CSO phase. However, the strongest XRD diffraction peaks of CSO-HH, CSO-CH, and CSO-CC are shifted in different directions with respect to the strongest diffraction peak of the pure α'L-CSO phase. From the viewpoint of ionic radius, the radius of Eu^{2+} (r_{10} = 1.35 Å, r_8 = 1.25 Å) is smaller than that of Sr^{2+} (r_{10} = 1.36 Å) and larger than that of Ca^{2+} (r_8 = 1.12 Å). When Eu^{2+} replaces larger Sr^{2+} or smaller Ca^{2+}, the diffraction peaks will be shifted to higher or lower angles due to the lattice contraction or expansion, respectively. Therefore, these XRD results imply that there are variations in the distribution of Eu^{2+}. For the hydrogen-reducing atmosphere (CSO-HH), Eu^{2+} mainly occupies the Sr^{2+} site, causing the XRD diffraction peaks to be shifted to a higher 2θ angle. Yet in the thermal carbon-reducing atmosphere (CSO-CC), Eu^{2+}

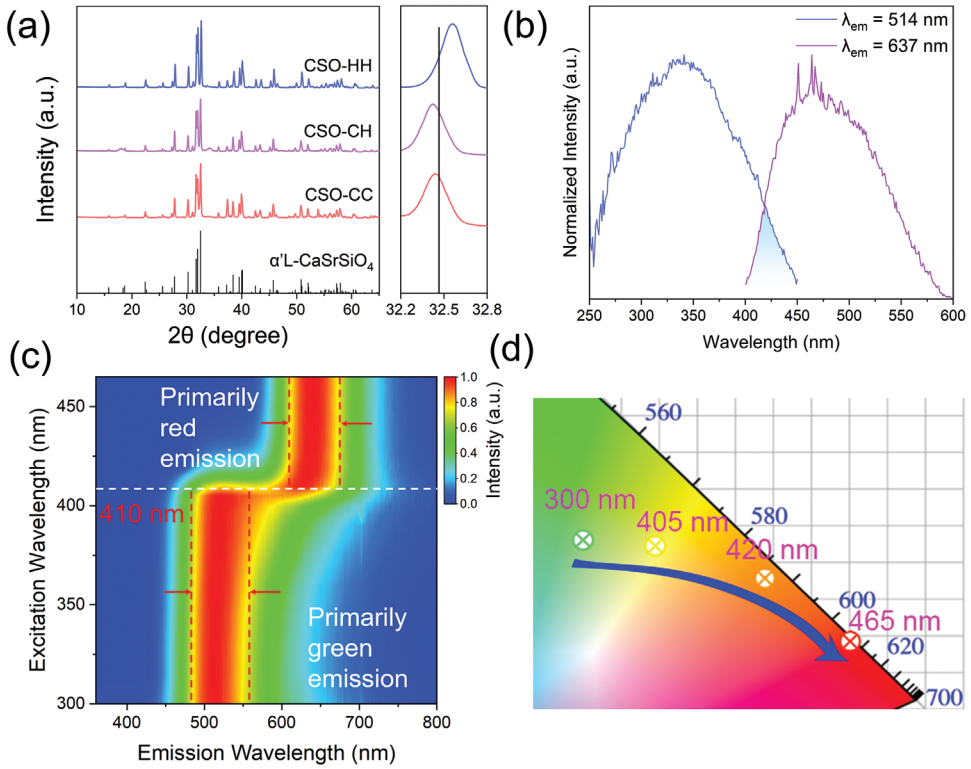

Figure 2. a) XRD patterns of CSO:0.015Eu^{2+} phosphors. The right inset is the magnified XRD patterns in the region of 32.2°–32.8°. b) PLE spectra of CSO-CH monitored at 514 and 637 nm. c) Excitation wavelength-dependent PL spectra of CSO-CH. d) CIE chromaticity coordinates of CSO-CH at different excitation wavelengths.

is distributed in the Ca^{2+} site, which leads to a low-angle shift of the diffraction peaks. As for CSO-CH, the diffraction peaks of CSO-CH are more significantly shifted to lower angles than CSO-CC. It is pointed out that, compared to CSO-CC, CSO-CH exists with fewer Eu^{3+} (This is confirmed in the later content). The small ionic radii of Eu^{3+} (r_8 = 1.07 Å) slow down the tendency of CSO-CC to shift to lower angles. Besides, as a result of this difference in the distribution of Eu^{2+}, the cell volume and average ionic radius of the samples obtained by Rietveld refinement show a corresponding trend (Figure S9 and Table S1, Supporting Information). The cell volume and average ionic radius of CSO-HH are smaller than these of the pure matrix (CSO). While the cell volumes and average ionic radius of both CSO-CH and CSO-CC are larger than these of CSO. Also, disturbed by Eu^{3+}, the cell volume and average ionic radius of CSO-CC are only slightly larger than those of CSO-CH. Furthermore, this distribution regularity of Eu^{2+} is also reflected in the doping concentration-dependent PL emission spectra (Figure S10, Supporting Information). The longer wavelengths of red emission arise when higher contents of Eu^{2+} occupy the Ca^{2+} site. As a result, CSO-CC exhibits red emission at longer wavelengths than CSO-HH under 465 nm excitation (Figure S7, Supporting Information). The above results convey that the reducing atmosphere can induce the site-selective occupation of Eu^{2+} at either Sr^{2+} sites or Ca^{2+} sites. Under the strongly reducing atmosphere (hydrogen), Eu^{2+} selectively occupies the Sr^{2+} site (CSO-HH), while under the weakly reducing atmosphere (thermal-carbon), Eu^{2+} is mainly located at the Ca^{2+} sites (CSO-CC). Unfortunately, the distribution of Eu^{2+} on either the three Sr^{2+} or the three Ca^{2+} sites is indistinguishable even at low temperatures (≈78 K) due to the similar local coordination environment of the three kinds of Sr^{2+} or the three kinds of Ca^{2+} sites (Figures S11 and S12, Supporting Information).

In addition to different emission characteristics, Eu^{2+} exhibits distinct excitation characteristics at Sr^{2+} and Ca^{2+} sites. As shown in Figure 2b, the excitation wavelength of Eu^{2+} at the Sr^{2+} site is 250–450 nm, while the excitation range of Eu^{2+} at the Ca^{2+}site is 400–600 nm. It is worth mentioning that for Eu^{2+}-activated phosphors with multiple luminescence centers, there is usually a significant overlap in the excitation spectra due to the similar coordination environment and the interaction between Eu^{2+} at different lattice sites.[13a,18] Herein, Eu^{2+} ions either at the Sr^{2+} or Ca^{2+} sites possess independent excitation characteristics, implying that the Eu^{2+} at each of these two different types of sites have optical properties that do not interfere with each other. The simultaneous distribution of Eu^{2+} in these two different types of sites enables a wide range of multi-color tunable output by tuning the excitation wavelength. As displayed in Figure 2c, it is noticed that the luminescence of the CSO-CH exhibits a pronounced excitation wavelength-dependent behavior. As the excitation wavelength increases, the intensity ratio of red to green emission gradually rises. The green emission is stronger than the red emission under short-wavelength excitation (λ_{ex} < 410 nm). In contrast, the red emission is stronger than the green emission under long-wavelength excitation (λ_{ex} > 410 nm). Under 410 nm excitation,

the green and red emissions are nearly equal in intensity (Figure S13, Supporting Information). The emission peak is composed almost exclusively of the red emission band when the excitation wavelength exceeds 450 nm. More visualized luminous color tunability of CSO-CH from green to red by modulating the excitation wavelength is observed in CIE chromaticity coordinates (Figure 2d).

The samples were prepared under the same experimental conditions, including the identical raw material ratio, sintering temperature, heating rate, etc., except for the different reducing atmospheres. The difference in reduction atmosphere is found directly affect the extent of Eu^{3+} reduction. As illustrated in **Figure 3**a, under excitation at 394 nm, CSO-CC shows distinctive emission peaks of Eu^{3+}-$^5D_0$ to ^7F_J (J = 1, 2, 4) transitions at around 588, 612, and 703 nm. Compared to CSO-CC, the intensity of the Eu^{3+} emission peak of CSO-CH is significantly weakened while the green emission of Eu^{2+} is enhanced, indicating that some of the Eu^{3+} ions are further reduced under the hydrogen atmosphere. Most of the europium ion in CSO-HH is reduced to Eu^{2+}, thus CSO-HH shows strong green emission of Eu^{2+} and weak red emission of Eu^{3+}. The XPS results reveal similar information (Figure S14, Supporting Information). The variation in the intensity ratio of the XPS peaks of Eu^{3+} $3d_{5/2}$ and Eu^{2+} $3d_{5/2}$ in the samples is presented in Figure 3b. CSO-CC displays the largest intensity ratio (Eu^{3+} $3d_{5/2}$/Eu^{2+} $3d_{5/2}$), followed by CSO-CH, and the smallest by CSO-HH. Furthermore, the valence state variation of europium ions induced by the reducing atmosphere is demonstrated by the X-ray absorption near-edge structure (XANES). The Eu-L_3 edge XANES spectra of samples are presented in Figure 3c. The two signals located at 6974 and 6982 eV are assigned to $2P_{3/2} \rightarrow 5d$ electron transitions of Eu^{2+} and Eu^{3+}, respectively.[19] The spectra reveal that the Eu^{3+} content in CSO-CC is higher than that in CSO-CH and CSO-HH. The reduction effect of the hydrogen atmosphere is better than that of the thermal carbon-reducing atmosphere, thus Eu^{3+} is reduced to a higher degree under the hydrogen-reducing atmosphere.

The different residual amounts of Eu^{3+} and significant differences in optical properties in the samples under different reducing atmospheres infer that Eu^{3+} may play a key role in the distribution of Eu^{2+} in the CSO. To confirm this conjecture, a validation experiment was carried out. The samples were reduced under thermal carbon-reducing atmospheres, one with a more carbon block (CSO-CC) and the other with a less carbon block (named CSO-CC-less). More Eu^{3+} is present in CSO-CC-less because the decrease in the carbon block leads to less CO being produced, and decreasing degree of reduction of Eu^{3+} (Figure S15, Supporting Information). As mentioned above, Eu^{2+} at both Sr^{2+} and Ca^{2+} sites can be excited by 420 nm, so the PL emission spectra of CSO-CC and CSO-CC-less under 420 nm excitation are detected for the analysis of optical properties (Figure 3d). The emission spectrum of CSO-CC contains both green and red emission bands, while CSO-CC-less exhibits only a single red emission band. This

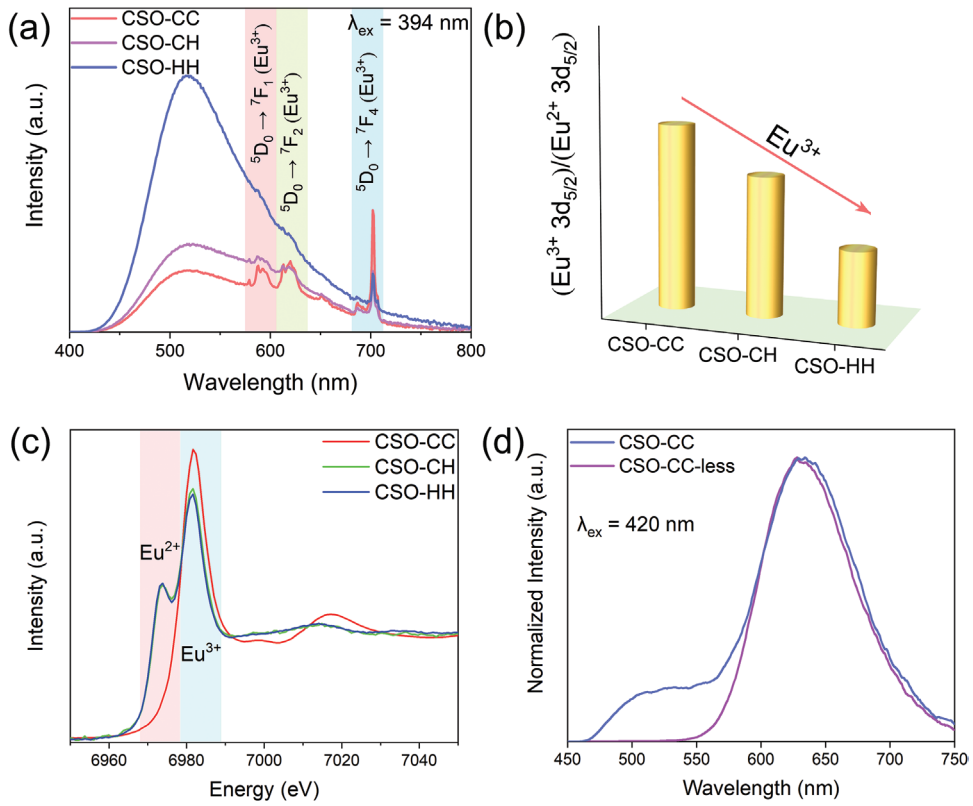

Figure 3. a) PL emission spectra of CSO:0.015Eu^{2+} phosphors under 394 nm excitation. b) XPS peak intensity ratios of Eu^{3+} $3d_{5/2}$ and Eu^{2+} $3d_{5/2}$ in CSO-HH, CSO-CH, and CSO-CC. c) Eu L3-edge XANES spectra of CSO-HH, CSO-CH, and CSO-CC. d) PL emission spectra of CSO-CC and CSO-CC-less under 420 nm excitation.

result implies that Eu^{2+} in CSO-CC-less is almost entirely occupied at the Ca^{2+} site. The weakening of the reducing atmosphere leads to more residual Eu^{3+}. The unreduced Eu^{3+} further helps to break the Eu^{2+} propensity to occupy the Sr^{2+} site and induces Eu^{2+} into the Ca^{2+} site, resulting in most of the Eu^{2+} preferentially occupying the Ca^{2+} site corresponding to the predominant red emission.

In order to further verify the effect of Eu^{3+} on the site occupation of Eu^{2+}, the formation energy was calculated by DFT+*U*. The formation energy of Eu^{2+} at different cationic sites was first calculated when only Eu^{2+} is in the α'L-CSO crystal structure. The lower formation energy of Eu^{2+} in Sr1, Sr2, Sr3, and Ca3 sites supported the major and minor distribution of Eu^{2+} in Sr and Ca sites (**Figure 4**a), respectively, in line with the predominant green emission of CSO-HH. Before investigating the effect of Eu^{3+} on the site occupation of Eu^{2+}, the location of Eu^{3+} was analyzed, and the result implies that Eu^{3+} ions tended to occupy the Sr^{2+} sites (Figure 4b). Further, the effect of Eu^{3+} on the site-selective occupation of Eu^{2+} was analyzed. The existence of Eu^{3+} increases the formation energy of Eu^{2+} substituting Sr ions, indicating Eu^{3+} helps Eu^{2+} enter into the Ca sites of red emission (Figure 4c). Based on theoretical calculations, it was found that Eu^{2+} preferentially enters the Sr^{2+} site in the absence of Eu^{3+}, while Eu^{3+} contributes to the Eu^{2+} entry into the Ca^{2+} site in the presence of Eu^{3+}. The above experimental analysis and theoretical calculations show that Eu^{3+} plays a crucial role in the distribution of Eu^{2+} in α'L-CSO.

The interfering role of residual Eu^{3+} in the distribution of Eu^{2+} is further elucidated in the view of the structure. A possible mechanism for reducing atmosphere-induced site-selective occupation of Eu^{2+} is shown in Figure S16, Supporting Information. In the absence of Eu^{3+} (hydrogen atmosphere), Eu^{2+} will prefer to occupy the Sr^{2+} site due to the fact that Eu^{2+} and Sr^{2+} have the same valence and almost the identical ionic radius (CSO-HH). In the presence of Eu^{3+} (thermal-carbon), the unreduced Eu^{3+} will preferentially enter the Sr^{2+} site (as shown in Figure 4b). The aliovalent substitution of the small ionic radius Eu^{3+} for the large ionic radius Sr^{2+} will form cationic vacancies (V_{cat}), leading to a local contraction of the outer SrO_{10} polyhedrons. In consequence, the central CaO_8 polyhedron neighboring the outer locally contracted SrO_{10} polyhedron will become looser to minimize the lattice strain, which creates an opportunity for Eu^{2+} to enter the Ca^{2+} site (Figure 4d). Thus, Eu^{2+} will be gradually distributed to the Ca^{2+} site (CSO-CH and CSO-CC). Eu^{2+}, which occupies the Sr^{2+} and Ca^{2+} sites, possesses quite different optical properties. Eu^{2+} occupying the Sr^{2+} site emits green light under 250–450 nm excitation, while Eu^{2+} in the Ca^{2+} site emits red light under 400–600 nm excitation (Figure 4e). CSO-HH exhibits mainly green emissions under UV excitation stemming from the fact that Eu^{2+} is mainly distributed in the Sr^{2+} site. CSO-CC presents red emission under blue light excitation due to the fact that Eu^{2+} is mainly distributed in the Ca^{2+} site. As for CSO-CH, Eu^{2+} is relatively uniformly distributed in the Sr^{2+} and Ca^{2+} sites and

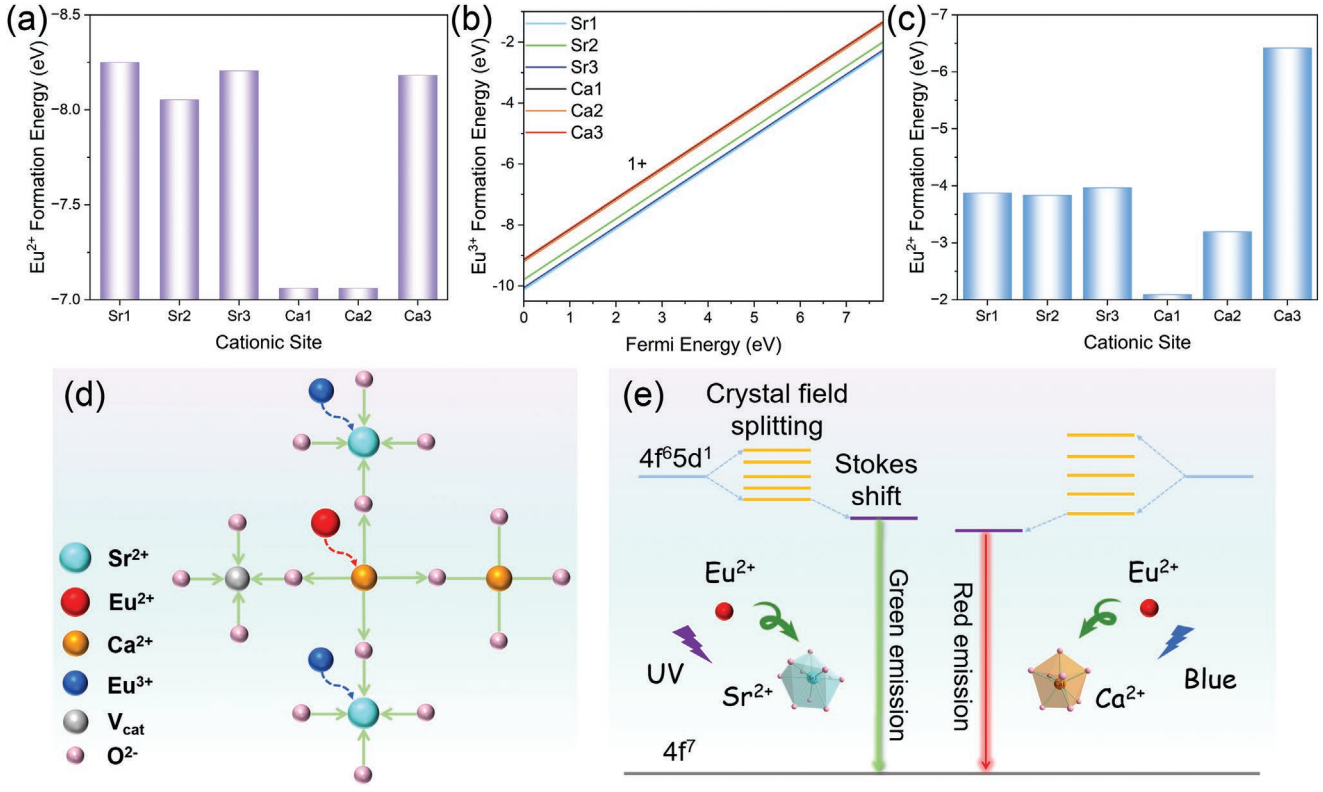

Figure 4. a) Formation energy of Eu^{2+} substitution for cationic sites (Sr^{2+} and Ca^{2+} sites). b) Formation energy of Eu^{3+} substitution for cationic sites as a function of Fermi energy. c) Formation energy of Eu^{2+} substitution for cationic sites in the presence of Eu^{3+}. d) Schematic diagram of the regulation mechanism of site-selective occupation of Eu^{2+} by Eu^{3+}. e) Schematic illustration of the optical features corresponding to Eu^{2+} at the Sr^{2+} and Ca^{2+} sites.

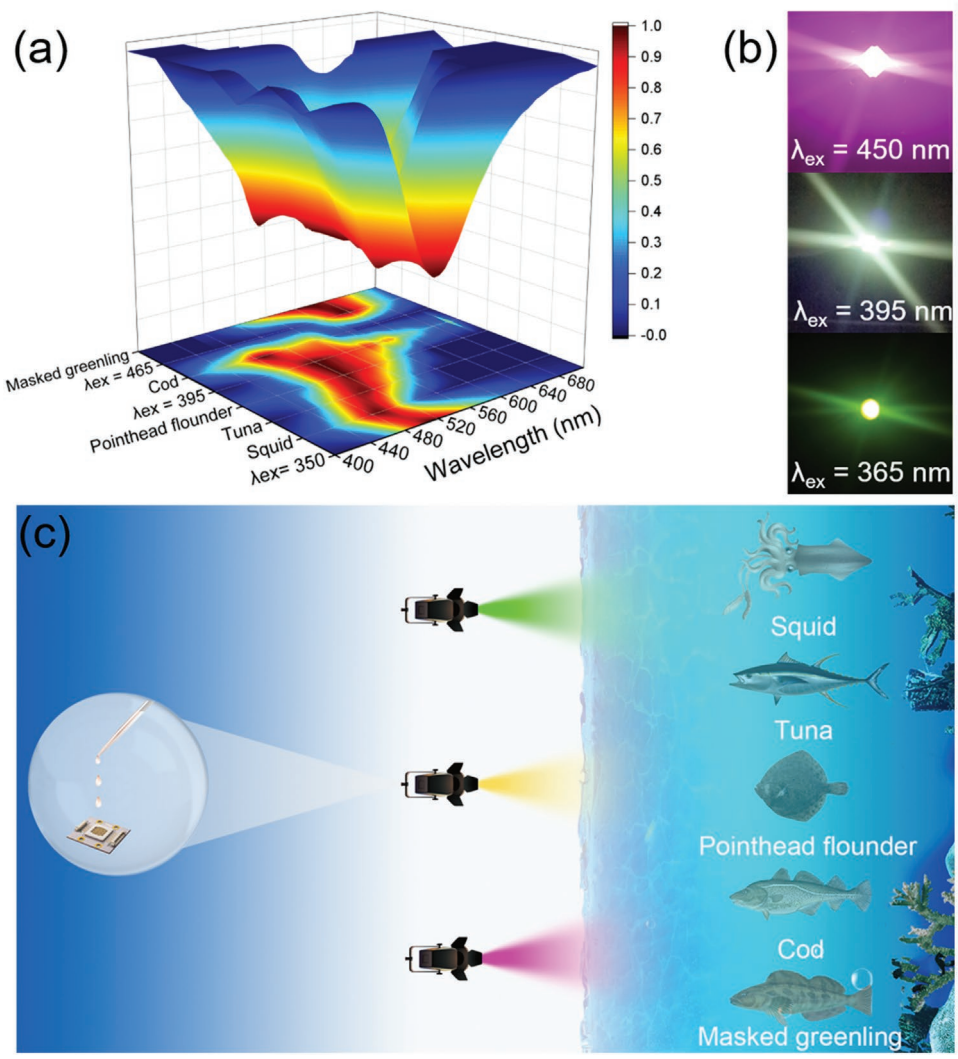

Figure 5. a) Light sensitivity spectra of squid, tuna, pointhead flounder, cod, and masked greenling, as well as the emission spectra of CSO-CH phosphor at 350, 395, and 465 nm excitation. b) LEDs fabricated by CSO-CH phosphor. c) Schematic diagram of CSO-CH phosphor applied to the fish-attracting lamp.

thanks to the optical property of non-interference between Eu^{2+} on Ca^{2+} and Sr^{2+} sites, CSO-CH exhibits a wide range of multi-color output capability by adjusting the excitation wavelength.

The attractive dynamic multi-color tunable performance of CSO-CH grants it great potential for application in fish-attracting lamps. The natural phototropism of fish can be exploited to enable more efficient fishing. The tunable color range of CSO-CH already covers most of the spectral sensitivity regions of most marine fish (**Figure 5**a). Based on the CSO-CH phosphor, LED devices were fabricated (Figure 5b). Compared with traditional fish-attracting lamps, CSO-CH application in a fish-attracting lamp can ensure more energy-saving and more productive fishing by flexibly emitting the required light color according to actual requirements while avoiding unnecessary light loss (Figure 5c). This single-phase phosphor with multi-excitation and emission characteristics offers the possibility of developing higher-quality next-generation fish-attracting lamps and other innovative optical devices.

3. Conclusions

In summary, we propose a crystal-site engineering method that regulates the distribution of a single activator (Eu^{2+}) in a single-phase host matrix ($SrCaSiO_4$) by simply reducing atmosphere modification. Based on this approach, three CSO:Eu^{2+} phosphors with different optical properties were synthesized. CSO-HH shows green emission under UV excitation because Eu^{2+} is almost distributed in the Sr^{2+} site, while Eu^{2+} in CSO-CC occupies mainly the Ca^{2+} site and thus presents red emission under blue light excitation. And further, owing to the relatively balanced distribution of Eu^{2+} in both Sr^{2+} and Ca^{2+} sites and the optical property that Eu^{2+} in both sites do not interfere with each other, which endows CSO-CH phosphor with a wide range of multi-color output capability from green to yellow to red light by altering the excitation wavelength. Both theoretical analysis and experimental verification point to the residual Eu^{3+} inducing migration of Eu^{2+}

from the preferentially selectively occupied Sr^{2+} site to the Ca^{2+} site. Benefiting from the unique optical properties, the tunable color range of CSO-CH phosphor covers the spectral-sensitive region of most marine fish, which suggests the potential application value of this phosphor in higher-quality next-generation fish-attracting lamps.

4. Experimental Section

The detailed materials and synthesis, measurement and characterization, and theoretical calculation are available in the Supporting Information.

Supporting Information

Supporting Information is available from the Wiley Online Library or from the author.

Acknowledgements

This work was financially supported by grants from the National Natural Science Foundation of China (NSFC, no. 51902355, and 52002411) and its joint project with Yunnan (no. U1702254) and Guangdong (no. U1801253) Provinces, and the GDAS' Project of Science and Technology Development (no. 2022GDASZH-2022010104). The authors are grateful to Prof. Ru-shi Liu for the in-depth communication and valuable advice on the improvement of the manuscript.

Conflict of Interest

The authors declare no conflict of interest.

Data Availability Statement

The data that supports the findings of this study are available in the supplementary material of this article.

Keywords

crystal-site engineering, fish-attracting lamps, multi-emission, multi-excitation, single-phase phosphors

Received: December 31, 2022
Revised: February 13, 2023
Published online: March 12, 2023

[1] K. Q. Nguyen, P. D. Winger, *Rev. Fish. Sci. Aquacult.* **2019**, *27*, 106.
[2] a) F. Li, C. Hua, Q. Zhu, L. Song, *Fish. Sci.* **2021**, *87*, 283; b) G. Telemka, M. Mghamba, A. Ntarisa, *Circuits Syst.* **2018**, *09*, 67.
[3] a) D. Lee, K. Lee, Y. Pyeon, S. Kim, J. Bae, *J. Korean Soc. Fish. Ocean Technol.* **2015**, *51*, 163; b) S. C. Shen, C. Y. Kuo, M.-C. Fang, *Int. J. Adv. Rob. Syst.* **2013**, *10*, 183.
[4] a) Y. Li, W. B. Zheng, Z. Cui, *Hubei Agric. Sci.* **2017**, *56*, 2536; b) S. L. Kondrashev, *Vision Res.* **2008**, *48*, 2269; c) K. Matsuda, S. Torisawa, T. Hiraishi, K. Yamamoto, *Fish. Sci.* **2008**, *75*, 35.
[5] S. Musbir, M. Kurnia, *IOP Conf. Ser.: Earth Environ. Sci.* **2020**, *564*, 012075.
[6] a) P. Pei, R. Wei, B. Wang, J. Su, Z. Zhang, W. Liu, *Adv. Funct. Mater.* **2021**, *31*, 2102479; b) B. Zhou, L. Yan, J. Huang, X. Liu, L. Tao, Q. Zhang, *Nat. Photonics* **2020**, *14*, 760; c) C. Shi, X. Shen, Y. Zhu, X. Li, Z. Pang, M. Ge, *ACS Appl. Mater. Interfaces* **2019**, *11*, 18548; d) R. Deng, F. Qin, R. Chen, W. Huang, M. Hong, X. Liu, *Nat. Nanotechnol.* **2015**, *10*, 237; e) T. Si, Q. Zhu, T. Zhang, X. Sun, J.-G. Li, *Chem. Eng. J.* **2021**, *426*, 131744.
[7] a) M. Zhao, Z. Yang, L. Ning, Z. Xia, *Adv. Mater.* **2021**, *33*, 2101428; b) R. Gautier, X. Li, Z. Xia, F. Massuyeau, *J. Am. Chem. Soc.* **2017**, *139*, 1436.
[8] a) C. Yang, X. Chen, M. Mao, X. Luo, W. Sheng, Z. Lu, S. Sun, H. He, W. Su, K. Song, *Ceram. Int.* **2023**, *49*, 7683; b) C. Yang, C. Fan, F. Hussain, Z. Ye, W. Sheng, K. Song, R. Muhammad, J. Wu, Q. Huang, H. Wang, W. Su, J. Xu, S. Sun, D. Wang, *J. Alloys Compd.* **2022**, *902*, 163724.
[9] a) M. Zhao, Q. Zhang, Z. Xia, *Acc. Mater. Res.* **2020**, *1*, 137; b) M. Zhao, Q. Zhang, Z. Xia, *Mater. Today* **2020**, *40*, 246; c) D. Wu, C. Shi, J. Zhou, Y. Gao, Y. Huang, J. Ding, Q. Wu, *Chem. Eng. J.* **2022**, *430*, 133062.
[10] a) Y. Wei, L. Cao, L. Lv, G. Li, J. Hao, J. Gao, C. Su, C. C. Lin, H. S. Jang, P. Dang, J. Lin, *Chem. Mater.* **2018**, *30*, 2389; b) Z. Wang, J. Ha, Y. H. Kim, W. B. Im, J. McKittrick, S. P. Ong, *Joule* **2018**, *2*, 914; c) P. Pust, V. Weiler, C. Hecht, A. Tucks, A. S. Wochnik, A. K. Henss, D. Wiechert, C. Scheu, P. J. Schmidt, W. Schnick, *Nat. Mater.* **2014**, *13*, 891; d) J. Qiao, G. Zhou, Y. Zhou, Q. Zhang, Z. Xia, *Nat. Commun.* **2019**, *10*, 5267; e) Z. Yang, Y. Zhao, Y. Zhou, J. Qiao, Y. C. Chuang, M. S. Molokeev, Z. Xia, *Adv. Funct. Mater.* **2021**, *31*, 2103927.
[11] a) Y. Sato, H. Kato, M. Kobayashi, T. Masaki, D. H. Yoon, M. Kakihana, *Angew. Chem., Int. Ed.* **2014**, *53*, 7756; b) M.-H. Fang, C. O. M. Mariano, P.-Y. Chen, S.-F. Hu, R.-S. Liu, *Chem. Mater.* **2020**, *32*, 1748; c) X. Sheng, P. Dai, Z. Sun, D. Wen, *Chem. Eng. J.* **2020**, *395*, 125141; d) Y. Zhuo, S. Hariyani, J. Zhong, J. Brgoch, *Chem. Mater.* **2021**, *33*, 3304.
[12] a) W. Wang, M. Tao, Y. Liu, Y. Wei, G. Xing, P. Dang, J. Lin, G. Li, *Chem. Mater.* **2019**, *31*, 9200; b) D. Zhang, X. Zhang, B. Zheng, Q. Sun, Z. Zheng, Z. Shi, Y. Song, H. Zou, *Adv. Opt. Mater.* **2021**, *9*, 2100337; c) J. Qiao, Y. Zhou, M. S. Molokeev, Q. Zhang, Z. Xia, *Laser Photonics Rev.* **2021**, *15*, 2100392.
[13] a) R. Zhou, C. Liu, L. Lin, Y. Huang, H. Liang, *Chem. Eng. J.* **2019**, *369*, 376; b) P. Dang, G. Li, S. Liang, H. Lian, J. Lin, *J. Mater. Chem. C* **2019**, *7*, 5975; c) X. Wu, R. Shi, J. Zhang, D. Wen, Z. Qiu, X. Zhang, W. Zhou, L. Yu, S. Lian, *Chem. Eng. J.* **2022**, *429*, 132225.
[14] A. M. Il'inets, N. N. Nevsky, V. V. Ilyukhin, M. Y. Bikbau, N. V. Belov, *Dokl. Akad. Nauk SSSR* **1982**, *267*, 641.
[15] L. Zhou, W. Zhou, F. Pan, R. Shi, L. Huang, H. Liang, P. A. Tanner, X. Du, Y. Huang, Y. Tao, L. Zheng, *Chem. Mater.* **2016**, *28*, 2834.
[16] a) H.-J. Woo, S. Gandhi, B.-J. Kwon, D.-S. Shin, S. S. Yi, J. H. Jeong, K. Jang, *Ceram. Int.* **2015**, *41*, 5547; b) A. Mayavan, S. D. Krishnan, P. Rajendran, K. Jang, S. Gandhi, *Ceram. Int.* **2020**, *46*, 12216; c) S. Gandhi, K. Thandavan, B.-J. Kwon, H.-J. Woo, C. H. Kim, S. Yi, J. H. Jeong, D.-S. Shin, K. Jang, *J. Mater. Chem. C* **2014**, *2*, 6630; d) H. Zhang, Y. Song, Y. Sheng, K. Zheng, S. Ding, B. Yuan, X. Xu, H. Zou, *Opt. Mater.* **2015**, *47*, 143.
[17] J. Qiao, L. Ning, M. S. Molokeev, Y. C. Chuang, Q. Zhang, K. R. Poeppelmeier, Z. Xia, *Angew. Chem., Int. Ed.* **2019**, *58*, 11521.
[18] a) X. Zhang, J. Wang, L. Huang, F. Pan, Y. Chen, B. Lei, M. Peng, M. Wu, *ACS Appl. Mater. Interfaces* **2015**, *7*, 10044; b) L. Lin, L. Ning, R. Zhou, C. Jiang, M. Peng, Y. Huang, J. Chen, Y. Huang, Y. Tao, H. Liang, *Inorg. Chem.* **2018**, *57*, 7090.
[19] C. Cheng, L. Ning, X. Ke, M. S. Molokeev, Z. Wang, G. Zhou, Y. C. Chuang, Z. Xia, *Adv. Opt. Mater.* **2019**, *8*, 1901608.